



**HAL**  
open science

# Investigating the Young's modulus of Cu-Al-Be shape memory alloy using a phase diagram, vibration spectroscopy and ultrasonic waves

Rania Benlachemi, Erick Ogam, Nicholas Ongwen, Amar Boudour, Zine El Abiddine Fellah

## ► To cite this version:

Rania Benlachemi, Erick Ogam, Nicholas Ongwen, Amar Boudour, Zine El Abiddine Fellah. Investigating the Young's modulus of Cu-Al-Be shape memory alloy using a phase diagram, vibration spectroscopy and ultrasonic waves. *Journal of Alloys and Compounds*, 2024, 976, pp.173010. 10.1016/j.jallcom.2023.173010 . hal-04319556

**HAL Id: hal-04319556**

**<https://hal.science/hal-04319556v1>**

Submitted on 22 Nov 2024

**HAL** is a multi-disciplinary open access archive for the deposit and dissemination of scientific research documents, whether they are published or not. The documents may come from teaching and research institutions in France or abroad, or from public or private research centers.

L'archive ouverte pluridisciplinaire **HAL**, est destinée au dépôt et à la diffusion de documents scientifiques de niveau recherche, publiés ou non, émanant des établissements d'enseignement et de recherche français ou étrangers, des laboratoires publics ou privés.

# Investigating the Young's modulus of *Cu-Al-Be* shape memory alloy using a phase diagram, vibration spectroscopy and ultrasonic waves

Rania Benlachemi<sup>a</sup>, Erick Ogam<sup>b</sup>, Nicholas Ongwen<sup>c</sup>, Amar Boudour<sup>a</sup>, Z. E.A. Fellah<sup>b</sup>

<sup>a</sup>Laboratoire d'Elaboration et d'Analyse des Matériaux, Université BADJI Mokhtar Annaba, Algeria

<sup>b</sup>Laboratoire de Mécanique et d'Acoustique LMA - UMR 7031 Aix-Marseille Univ. - CNRS - Centrale Marseille

<sup>c</sup>Department of Physics and Materials Science, Maseno University, Maseno, Kenya.

---

## Abstract

This work presents a method for determining the effective Young's modulus ( $E_{effective}$ ) and Poisson ratio of small specimens of a ternary shape memory alloy (SMA), *Cu-Al-Be*. The alloys were synthesized uniformly and homogeneously using various concentrations of high purity metals and formed into slabs of different geometrical shapes. The phases and fractional quantities of each sub-alloy composing the SMA were determined using SEM/EDS data and the lever rule, and confirmed by matching computed and measured X-ray diffraction peak patterns. The  $E_{effective}$  was determined using the rule of mixtures, employing elastic moduli obtained from Ab initio (Density functional theory) calculations. To address the challenge of determining  $E_{effective}$  experimentally for small specimens, high frequency ultrasonic waves and vibration spectroscopy were used. The  $E_{effective}$  was then used in a 3D finite element model to compute the vibrational spectrum's resonance peaks, which were found to match those of the experimental vibrational response. The  $E_{effective}$  was also compared to the pressure wave (P-waves) modulus recovered using non-contact ultrasound waves propagating through the sample's thickness. Discrepancies mainly occurring for alloys with the  $\beta$  phase were resolved by determining its anisotropic spatial Young's modulus. Overall, the presented method provides a comprehensive characterization of the mechanical properties of small alloy specimens.

**Keywords:** Shape memory alloys, Elastic moduli, Phase diagram, Method of mixtures, Ab initio computation, Vibration spectroscopy, Ultrasonic waves

## 1. Introduction

Shape memory alloys (SMAs) represent a unique class of materials characterized by their remarkable ability to recover their original shape following significant and seemingly plastic deformation when exposed to specific stimuli, such as thermal processes. This exceptional property, known as the shape memory effect, has positioned SMAs as highly sought-after materials in a wide range of engineering applications. Furthermore, SMAs exhibit exceptional resistance to permanent deformation under high stresses, making them particularly well-suited for applications that demand both strength and durability.

The distinctive two-phase structure of SMAs, which imparts distinct properties to each phase, has garnered considerable attention and earned them recognition as intelligent materials. This inherent duality of properties has sparked interest in diverse fields, including biomedical devices, aerospace engineering, and robotics. Despite their well-established history spanning several decades, SMAs continue to captivate researchers and engineers alike due to their remarkable characteristics and ongoing potential for innovation. SMAs are elaborated by casting, using a vacuum arc melting or by induction melting. These specialist techniques are used in order to keep impurities in the alloy to a minimum, ensuring that the metals are well mixed. The ingot is often hot rolled into longer sections and then drawn into plates, rods or turned into wires, rings e.t.c. SMAs are used in several fields like in aerospace, civil engineering, and bioengineering (e.g., dental braces), in biomechanics (e.g., mending broken bones using metal plates).

In order to promote better mechanical properties, the SMA is heated into the austenite region and then quenched (heat extraction) in a bath maintained at a temperature within a desired range. The change in temperatures for the austenitization process can yield some desired microstructure. When the SMA is heated beyond  $A_s$  ( $s$  for start temperature) it begins to contract and transform into the austenite structure, recovering its original form [1]. The physical and mechanical properties of SMAs vary between these two phases such as (Young's modulus, electrical resistivity, thermal conductivity and thermal expansion coefficient). The austenite structure is relatively hard and has a much higher Young's modulus (YM); whereas the martensite structure is softer and

---

*Email address:* [ogam@lma.cnrs-mrs.fr](mailto:ogam@lma.cnrs-mrs.fr) (Erick Ogam)

more malleable. The differential scanning calorimetry (DSC) technique was used in this study to determine the phase transformations in SMAs studied.

The first of these phases can be induced by mechanical forces or by temperature changes in a cooling process from high temperatures (but takes place below the transition temperature) and is called martensite. This transformation is a shear-like mechanism which takes place below the transition temperature. The diffusionless nature and the resulting lattice change is a global lattice distortion at the unit cell level (atomic rearrangements). This phase change in SMAs is reversible. It is merely a shear lattice distortion, contrary to a typical transformation that involves the diffusion of atoms. When the SMA is heated to a temperature above the critical eutectoid temperature it changes its crystal structure from martensite ( $M$ ) to austenite ( $A$ ) [2]. The temperatures at which the material undergoes martensitic transformation and austenitic reversion, are also important factors in determining whether a material is a SMA or not.

To better understand SMAs and improve the quality of the finished product, new studies concerning their properties are necessary. The role of precipitates on the properties of austenite, martensite  $NiTi$  were studied in [3]. It was shown that coherent precipitates lowered the transformation stress at small strains while increasing the slip resistance of austenite and martensite domains at higher strains.

The relatively high cost of the first SMAs which were made from nitinol has led to studying the possibilities of using cheaper, copper-based alloys. In terms of cost comparison, for example, nickel-titanium alloys cost about US \$11 a pound, while copper-zinc-aluminium ( $Cu-Zn-Al$ ) alloys cost only about US \$1 a pound.

The addition of approximately 0.1% of beryllium ( $Be$ ) to  $CuAl$ , reduces these temperatures by about 100°C [4, 5, 6]. Beryllium and Copper provide the high mechanical strength that  $Cu-Al-Be$  alloys present when subjected to high pressure. Beryllium presents high stiffness to weight ratio that combined with its excellent damping properties makes  $Cu-Al-Be$  alloys excellent materials for acoustic applications [7]. The formed phases can be obtained theoretically by considering the binary alloy composed of  $Cu-Al$  only, since  $Be$  is in very small percentage quantity (see the phase diagram in Fig. 1). A  $Cu-Al$  phase diagram involving temperatures can be found in reference [8].

In this study we develop experimental methods (ultrasonic wave propagation and

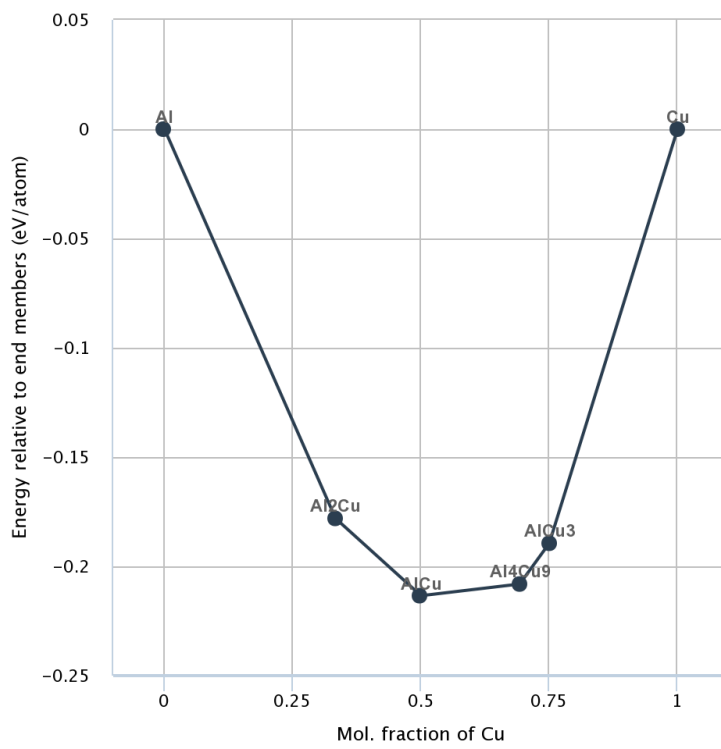


Figure 1: The Phase diagram for *Cu-Al* Computed with tools from Materials project [9].

vibration) and employ three dimensional (3D) finite element methods (FEM) steady state dynamic vibration analysis to study the vibrational response spectrum as a function of the effective elastic properties and Poisson ratios of the SMAs [10, 11]. The advantage of using vibration spectroscopy is that the samples can be of any shape (since they are then modeled using 3D FEM) and size. The retrieved elastic parameters are therefore those of the formed phases of *Cu-Al-Be* SMAs.

The composition of each formed sub-alloy phase in an SMA can be determined using data from the Energy-dispersive X-ray spectroscopy (EDS) in conjunction with a scanning electron microscope (SEM) to select the measurement positions. The Atomic percentage, the formation temperature are then used with the phase diagram. After drawing the tie line to get the phases present and their compositions, the lever rule is applied to give the relative amounts of the phases found [12]. By using the retrieved relative fractional quantities and applying the rule of mixtures, the effective Young's modulus can finally be found if the modulus of each sub-alloy phase is known.

Young's modulus can be determined using alternative techniques such as nanoindentation or by employing a universal testing machine with an extensometer and force sensor to measure applied loads and specimen elongation. However, these methods have the disadvantage of being destructive. Previous studies have extensively explored the determination of elastic constants in *Cu-Al-Be* alloy. Noteworthy references include Montecinos et al. [13], where the Young's modulus of *Cu-Al-Be* SMAs was determined using an impulse mechanical excitation technique on large-sized  $\beta$  phase, specifically 15.1 mm diameter extruded bars with varying microstructures. Additionally, Dealbuquerque et al. [5] conducted a study using ultrasonic waves to determine Young's modulus in  $\beta$  Cu-Al-Be samples with different grain sizes, revealing a significant dependence of Young's modulus on grain size. The elastic constants of the metastable  $\beta$  phase in a *Cu-Al-Ni* (SMA) has been studied by resonant ultrasound spectroscopy (RUS [14]. Furthermore, Recarte et al. [14] investigated the elastic constants of the metastable  $\beta$  phase in a *Cu-Al-Ni* SMA using resonant ultrasound spectroscopy (RUS). These prior investigations have laid the groundwork for our study, inspiring a focused inquiry into the *Cu-Al-Be* alloy's elastic properties. In this context, our research aims to build upon the existing knowledge base by employing advanced techniques and methodologies to precisely

determine the elastic constants of the *Cu-Al-Be* SMA. By leveraging a combination of experimental analyses and computational simulations, we seek to contribute novel insights that advance the understanding of this alloy's mechanical behavior, with potential implications for diverse technological applications. Through a meticulous exploration of the alloy's elastic properties, we aim to bridge the existing gaps in the literature and provide valuable contributions to the field of SMA research.

The mechanical properties of *Cu-Al* binary alloys have previously been investigated using the first-principles calculation based on density functional theory [15]. Also, different structure derivatives of  $\beta \rightarrow Cu_3Al$  compositions were studied using first principles methods and Quasi-Harmonic Approximation in which their formation energies, elastic constants and various elastic moduli were estimated [8]. In order to determine the elastic constant, the relationship between the variation in the energy density/stress and the strain [16] are often determined by use of a set of uniform deformations on the fully optimized unit cell of the structure. The stress and strain computations were the basis of the calculations using the Ab initio method in this work [17].

One of the challenges was the use of acoustic methods in order to characterize very small sized SMA samples. The smallness imposed that very short acoustic wavelengths and therefore, ultrasonic waves be employed. In this study ultrasonic waves and ultrasonic vibration spectroscopy were employed to characterize the SMAs. Small samples appeal to the measurements using vibration spectroscopy (VS) whereby they can be excited using very small and thin piezoelectric discs and the response measured using the same [11]. The samples need not be sculptured into canonic shapes (e.g., cylinders) since any shape can be modeled using 3D FEM [18]. Therefore the latter method was used to compute the theoretical vibrational response spectrum using the effective modulus. This response can be compared to those obtained from the vibration spectroscopy experiment spectrum obtained for an SMA of the same geometry.

It was also important to compare the results obtained herein with those in the published literature and point out the reasons for the discrepancies. Therefore a study to determine the anisotropy (directional Young's modulus) of the materials were undertaken using the stiffness constants results from the Ab initio (Density functional theory - DFT) computations.

The paper is organized as follows: In Section 2 we describe the shape memory alloys employed, the experimental and first principle computational methods used in this work. The main results and discussion are reported in Sections 4 and 5 according to the following sequence: determination using differential scanning calorimetry of phase transformation points, elastic constants determination using ultrasonic measurements and vibration spectroscopy and the first principles computation of elastic properties results. Finally, the conclusions are given in Section 7.

## 2. Experimental and theoretical Methods

### 2.1. Shape memory alloys analyzed in the study

Three types of *Cu-Al-Be* SMAs were analyzed. They were synthesized [4, 19] through an induction melting process using commercially available Cu alloy, high-purity aluminum (99.99%), and electrolytic copper. The melting process took place in a crucible under a nitrogen atmosphere. To obtain cylindrical ingots, the liquid alloy was poured in situ into copper molds. Subsequently, the polycrystalline ingots were homogenized at 750 °C and rapidly quenched in water at room temperature. Analysis of the resulting alloy compositions was performed using plasma emission spectroscopy, with a high accuracy of 0.02%. The particularity of the alloys was that the addition of a small percentage of beryllium to the alloy of a composition close to a eutectoid  $Cu_3Al$  caused a very significant drop in the characteristic temperatures of the martensitic transformation. For their synthesis, they first underwent a homogenization treatment for 15 min at 750 °C followed by quenching in water with the aim that the  $\beta$  phase be the starting phase. The  $\beta$  phase is of a composition similar to the stoichiometric composition  $Cu_3Al$ . The samples then underwent annealing treatment for 1/2 hour and 2 hours at 500 °C.

The monocrystals were produced using the modified Bridgman method [20]. The polycrystals were sealed in silica ampoules under vacuum. The ampoule was then placed in the furnace at 1120 °C. The furnace was raised at a constant speed of 11 mm/hour. The material, in its liquid state, started to solidify from the bottom. A seed formed and grew, giving rise to a single grain.

After the monocrystal formation, the transformation temperature  $M_s$  increased by a few



Alloy	Composition			Geometry			
	Cu %	Al %	Be %	length (mm)	width (mm)	thickness (mm)	radius (mm)
CAB4	88.07	11.50	0.43	17.4	14.4	3.25	-
CAB18	87.77	11.76	0.47	-	-	1.0	13.9
CAB24	87.49	12.04	0.47	-	-	4.0	14.3

Table 1: Percentage SMA Composition Table, presenting the measured concentrations of different elements in the alloy as percentages of the total composition and the following columns the geometries and dimensions of each SMA studied.

degrees, likely due to evaporation of Beryllium or Zinc. A temperature transformation gradient may also appear within the sample.

The alloys were labelled CAB4, CAB18 and CAB24. All except CAB4 whose phase transformations was blocked are supposed to be in austenite phase. The compositions of the SMA alloys studied are compiled in Table 1.

## 2.2. Determination of the temperature transformation points

The temperature transformation points of a SMA are one of the defining characteristics of the material. This confirms that the crystal structure of the SMA changes at the transformation points. The recovery of shape is due to a reversible phase transformation that occurs within the material at a specific temperature range. Thermograms were obtained using a Differential Scanning calorimeter (DSC) [21] to measure the difference between the heat flow from the sample and reference sides of a sensor as a function of temperature [22]. The basic principle underlying this technique is that when the sample undergoes a physical transformation, in this case phase transitions, more or less heat will need to flow to it than the reference to maintain both at the same temperature.

The device used in our work is a DSC 131 Evo apparatus (Setaram Instrumentation, France), which allows temperature scans between -170 °C and 750 °C at rates below 10 °C/min. In our study, we chose to work with sample masses ranging from 5 to 20 mg with a kinetic rate of 5 °C/min. This rate is sufficient to clearly highlight direct and inverse transformations, and it is low enough to maintain a good equilibrium between the crucible's (reference) temperature and that of the sample. The sample to be measured and the reference sample (empty crucible) are placed in a sealed chamber, swept by an

inert gas (argon or nitrogen), and temperature-regulated. The cell continuously measures the temperature difference between the tested sample and the reference crucible.

The DSC measurements were undertaken for all the three *Cu-Al-Be* ternary alloy samples and were carried out at temperature ranges between -40 °C and 100 °C.

### *2.3. The ultrasonic vibration spectroscopy method*

In our ultrasonic vibration spectroscopy experiment, we followed the setup described in the work by Daoud Chanbi [11]. The experiment involved the use of two thin piezoelectric transducer (PZT) discs, both having the same diameter. The first PZT disc, affixed to one face of the SMA sample, served as the exciter, generating vibrations within the material. Meanwhile, the second PZT disc, placed on the opposite face of the sample, acted as the sensor, capturing the spectral vibration response of the SMA specimen. The alloy sample was carefully positioned between this pair of PZT transducer discs.

For our experiment, we opted for Kingstate KPEG 110 PZT discs with a diameter of 20 mm. Extensive testing demonstrated that these specific PZT discs provided the most optimal response for the samples under investigation. This setup allowed us to comprehensively analyze the vibrational behavior of the SMA sample, providing valuable insights into its mechanical properties.

### *2.4. The three-dimensional finite element for steady state dynamic vibrational response*

The specimens are solicited mechanically and vibrate in response to the excitation. The phenomenon is described by the classical equations of the elastodynamics of continuous elastic media. The computations by means of 3D FEM code (Abaqus [23] version 6.14 – 5) for a variety of specimen shapes and sizes, involves the steady-state linear dynamic analysis that predicts the linear response of the SMA sample subjected to continuous harmonic excitation. A nodal unit force (Element type=C3D20R, 1666 elements) is applied at the edges of the specimen [24, 11]. The acceleration response was obtained from a unique nodal on the flat surface of the specimen where the experimental response is measured.

The specimens were mechanically stimulated, inducing vibrations in response to continuous harmonic excitation. The dynamic behavior of the specimens was analyzed

using classical equations of elastodynamics applied to continuous elastic media. To perform these simulations, we employed a 3D finite element method (FEM) approach using Abaqus software (version 6.14-5) [23]. The simulations encompassed a diverse range of specimen shapes and sizes, aiming to capture the SMA sample's response under mechanical excitation. Specifically, we conducted steady-state linear dynamic analyses, predicting the linear behavior of the SMA sample subjected to continuous harmonic excitation.

In our simulations, a nodal unit force was applied at the edges of the specimen, utilizing the C3D20R element type with a discretization involving 1666 elements. The choice of this element type and discretization scheme was meticulously made to ensure accurate representation of the SMA's mechanical response [24, 11]. The resulting acceleration response was obtained from a carefully selected nodal point on the flat surface of the specimen, mirroring the location where the experimental response was measured. It's important to note that while our simulations focused on the mechanical response, future investigations will explore the incorporation of crystallographic texture effects to further enhance our understanding of the SMA's behavior under varying loading conditions. The effective Young's modulus were obtained using the methods to be described below. The 3D FEM vibrational response spectrum was first computed, then it was compared to the experimental vibrational response spectrum. There was validation if the resonance peaks in the two spectra matched one another [10, 11, 25].

The density of the SMA samples were obtained from measurements of their geometrical volumes and weights from on an electronic balance.

### *2.5. Ultrasonic measurement method in a water tank*

A non contact ultrasonic method to determine the time of flight within the thickness of a flat faced sample immersed in a water tank was employed in this study[26]. This was in order to obtain the P-wave modulus of the SMA samples. The challenge posed by the method was to achieve precision measurements of the ultrasonic wave propagation speed in the small sized samples of the SMAs without contact with the transducers. The small size of the samples dictated the use of a very high frequency (small wavelength and directive beam) transducer to limit the effects of edge diffraction. The SMA samples were attached using nylon threads then suspended in a water tank. This was to avoid stray reflections that may take place when the incident waves impinge on a massive support

that may have been used to suspend the samples in a water tank. The schematic of the experimental setup is shown in Figure (2).

In order that the samples thickness be considered small vis a vis the surface dimensions (length and width), a high frequency immersion transducer employed was a 50 MHz (model V358/50/0.25) connected to a pulser (Model 5073PR Olympus) both manufactured by Panametrics (Waltham USA). The signals were digitized without averaging using an Agilent oscilloscope. The velocity ( $v$ ) is related to the time of flight ( $t_{tof}$ ) by the following formula

$$v = \frac{2 * L}{t_{tof}} = \sqrt{\frac{M}{\rho}}, \quad (1)$$

where  $L$  is the thickness of the specimen,  $E$  is Young's modulus,  $\rho$  is the density,  $\nu$  the Poisson ratio,  $M$  is the P-wave modulus and is related to  $E$  and  $\nu$  through the relationship.

$$M = \frac{E(1 - \nu)}{(1 - 2\nu)(1 + \nu)}. \quad (2)$$

The P-wave modulus gives indication of the hardness and stability of the alloys.

### 3. Ab initio computational details

Ab initio (Density functional theory) calculations were undertaken in order to determine the directional as well as the global Young's moduli of the identified phases ( $\beta$ ,  $\varepsilon_2$  and  $\gamma_2$ ) of the SMA alloys. These were then employed to compute the effective Young's modulus used in the 3D steady state dynamic computation of the vibrational response spectrum. This spectrum was afterward compared to the vibrational experimental one to see whether the resonance peaks coincided. The goal was also to examine the reasons why the values of the Young's moduli of the *Cu-Al-Be* SMA obtained from previously reported experimental studies were lower than expected [13].

#### 3.1. Structural optimization

First-principles calculations were performed using Quantum espresso (QE) code [27]. Since *Be* was in very small quantities, *Al* and *Cu* were the only elements used in the

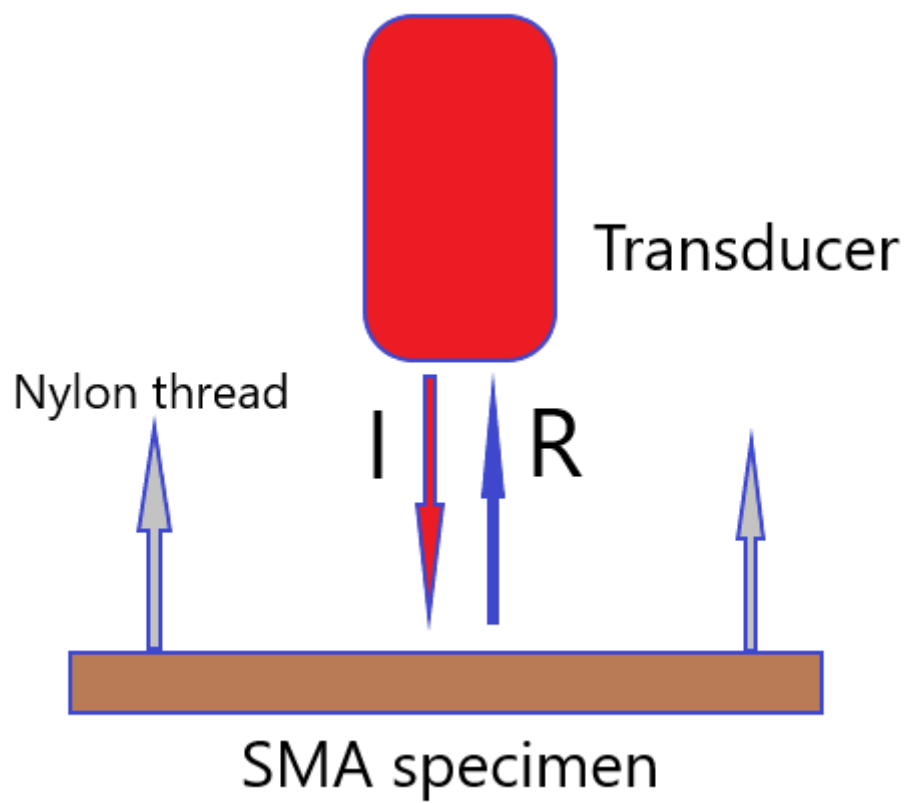


Figure 2: The schematic for the setup of the ultrasonic wave speed within the SMA layer sample measurement system sample immersed in a water tank.

SMA Alloy Phase	No. of atoms	
	<i>Al</i>	<i>Cu</i>
$AlCu_3$	8	24
$Al_4Cu_9$	10	22
$AlCu_{15}$	2	30

Table 2: The percentage composition of the elements in the two supercells together with the actual number of atoms.

doping process. The doping started with a copper (*Cu*) unit cell (Fig. 3a), which adopts a simple cubic structure with Fm-3m space group (number 225), consisting of 4 atoms. A 2 x 2 x 2 supercell was then created, which consisted of 32 atoms. The supercells were then doped (substitutional doping) by replacing some of the Cu atoms with atoms of aluminium (*Al*) (Table 2). Fig. 3 shows the simple cell of Cu and the two doped supercells. The experimental lattice parameter was 6.8321 a.u for the simple cell and 13.6642 a.u for the supercells.

### 3.2. Calculation of elastic constants

In the calculation of elastic constants, the stress-strain method [17] was employed within the generalized gradient approximation in the QE code. Small strains were applied to the crystal so as to remain within the linear regime of the Hooke's law (<1%). The strains applied were  $\pm 0.008$  in steps of 0.004 for the calculations (a total of 5 data points in each calculation). From the elastic stiffness and elastic compliance data, the polycrystalline bulk modulus (B), shear modulus (G), Young's modulus (E) and Poisson's ratio, were calculated using the Voigt approximation, which describes the upper bound and the Reuss approximation, which describes the lower bound. The average of the two approximations is called the Hill's approximation [28]. Two distortion matrices, which are sufficient for finding the 3 elastic stiffness constants ( $c_{11}$ ,  $c_{12}$  and  $c_{44}$ ) for the cubic crystals, were generated. The distortion matrices  $D_n$  ( $n = 1, 2$ ) are given in [29]. From the distortion matrices,  $c_{11}$  and  $c_{12}$  are obtained from the stress matrix of the output file of  $D_1$ . That is, the elastic stiffness  $c_{11}$  is obtained from the first element of the diagonal of the stress matrix while  $c_{12}$  is obtained from the second member of the diagonal element. The remaining elastic stiffness constant ( $c_{44}$ ) is obtained from the output of the second

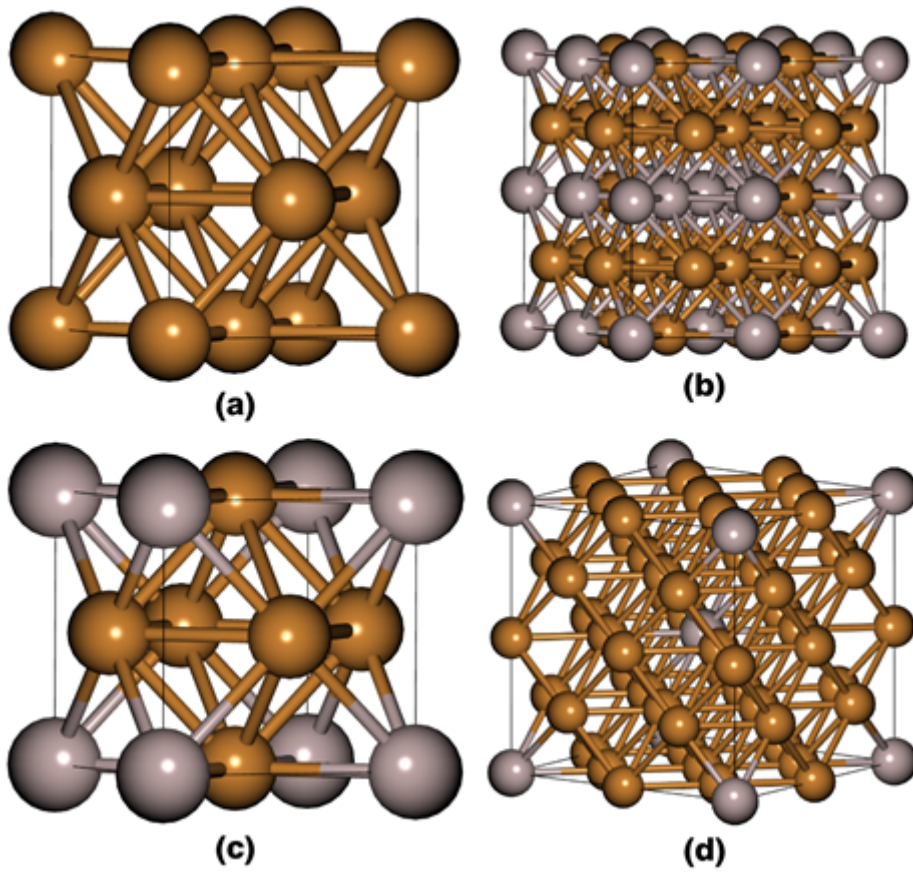


Figure 3: 3-D structures showing the atoms in the  $Al - Cu$  cells. (a) the original simple cubic Cu cell, (b) the doped supercell of  $AlCu_3$ , and (c) the supercell of  $Al_4Cu_9$  (d) the supercell of  $AlCu_{15}$  as viewed in Burai, a graphical user interface for Quantum Espresso program [27].

Alloy	Transformation points			
	$M_s$ (°C)	$M_f$ (°C)	$A_s$ (°C)	$A_f$ (°C)
CAB4	-	-	-	-
CAB18	4	-15	-6	13
CAB24	9	-15	2	17

Table 3: The phase transformation points for CAB4, CAB18, and CAB24 determined using DSC.

distortion matrix of  $D_2$ .

## 4. Results

### 4.1. Determination by DSC of phase transformation points and the corresponding (Effect of heat treatments on mechanical properties)

The differential scanning calorimetry (DSC) curves for three specimens are shown in Figure (4).

The four transformation points, namely  $M_s$ ,  $M_f$  (where the subscripts  $s$  and  $f$  represent the initiation and completion temperatures of the martensite phase transformation), and  $A_s$ ,  $A_f$  (denoting the onset and conclusion of the austenite phase transformation), were established. The DSC curves for the alloy CAB24 depicting plots of the heat treatment temperature versus time exhibited an endothermic peak during heating. This is a characteristic of the austenitic phase. It shows an exothermic peak during cooling but this characteristic of the martensite. The measured transformation points obtained are given in Table (3). From these points, it can be concluded that at room temperature, CAB24 is in the austenitic state. The alloy, CAB4, also exhibits the austenitic state, as can be observed in the optical images presented in the next section (subsection 4.2). This shows that CAB4 is a polycrystal which is in the austenitic state. Similarly, the CAB18 alloy exhibits austenitic behavior at room temperature and its  $M_s = 4$  °C (see Table 3). This will be further elucidated by the optical images provided in the subsequent section (subsection 4.2).



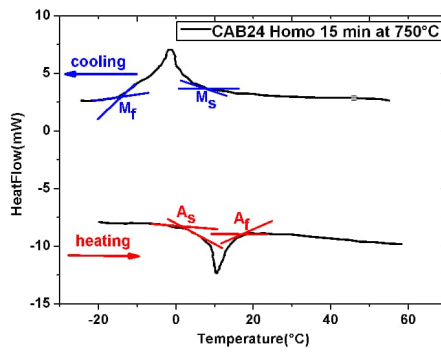
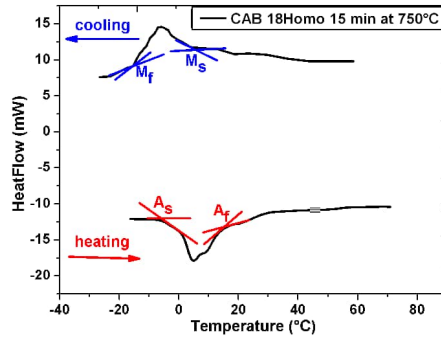
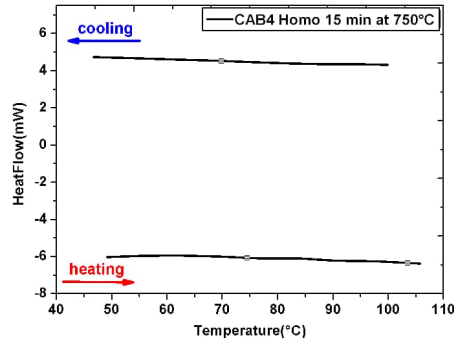


Figure 4: Differential Scanning Calorimetry for the three alloys (a) CAB4, (b) CAB18, (c) CAB24.  $A_s$  and  $A_f$  represent the start and finish of the phase transformations, and  $M_s$  and  $M_f$  denote the martensite phase transformations.

#### 4.2. Optical images of the CAB microstructure after different heat treatments

To identify the nature and grain size of the alloy phases present in the samples, the metallography analysis was done using an optical microscope (Axiovision, Carl Zeiss Microscopy, NY, USA) [2].

The Optical microscope images for the SMAs (CAB4, CAB18, CAB24) after heat treatments are depicted in Tables 4, 5, and 6. The histograms for grey color level of the pixels obtained after transformation of the color images to grey, indicate the presence of microstructural features like grain boundaries, precipitates, the separation of phases based on the peaks and valleys in the distribution. This is partly well demonstrated for CAB24 (Table 6).

Analysis of the DSC curves, showed that the transformation for CAB4 was blocked because there were no endo nor exothermic peaks during heating and cooling of the alloy. The optical images of this alloy (Table 4 uppermost panel) shows that it is a polycrystal. Following the annealing treatment of 1/2 hour at 500 °C (Table 4 middle panel), an enlargement of the grains with the appearance of a few precipitates in globular form which are called  $\alpha$  precipitates are observed. Subsequent treatment for 2 hours at 500 °C, results in the continuation of grain growth and the appearance of the observed  $\alpha$  precipitates.

The DSC curve for CAB18 provides the transformation points depicted in Table (3). From the observed points, it can be deduced that CAB18 is in its austenitic phase. Using optical observation, it can be deduced that this alloy is a polycrystal. After 2 hours at 500 °C, precipitates which were in their dendritic form called  $\gamma_1$  ( $Cu_9Al_4$ ) precipitates, appeared.

The optical microscope images of the CAB24 alloy (Table 6 uppermost panel) shows that it is a single crystal. Recall that the DSC measurement of the transition temperature  $M_s$  obtained for this alloy was 9.0 °C.

#### 4.3. SEM images, EDS X-ray and ab initio computations

Energy dispersive X-ray spectroscopy and quantitative backscattered electron imaging were used to analyze the phases formed and identify their composition and quantify the atomic percentage in each phase. This allows to distinguish between austenitic  $\beta_1$ -phase,

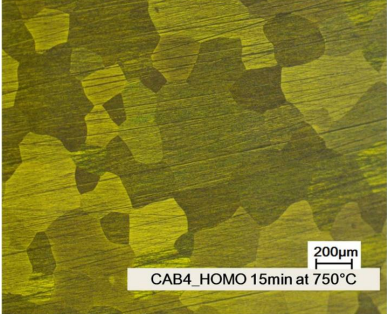
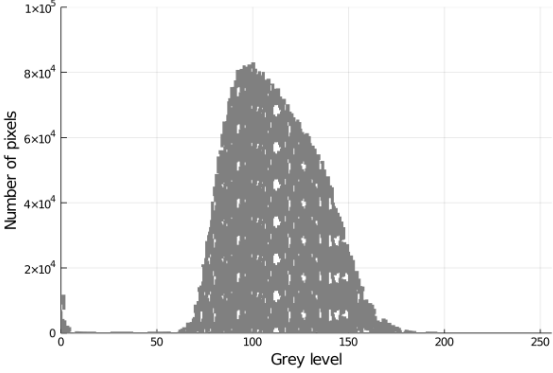

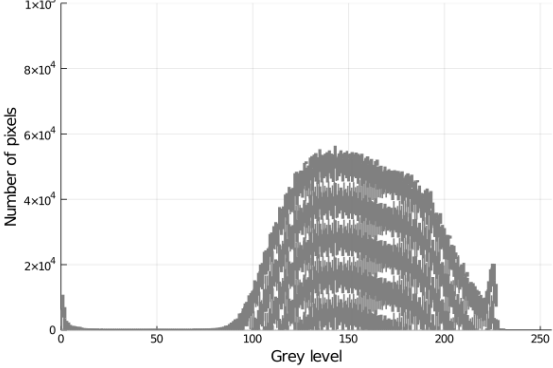
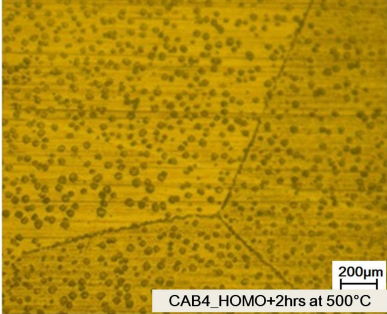
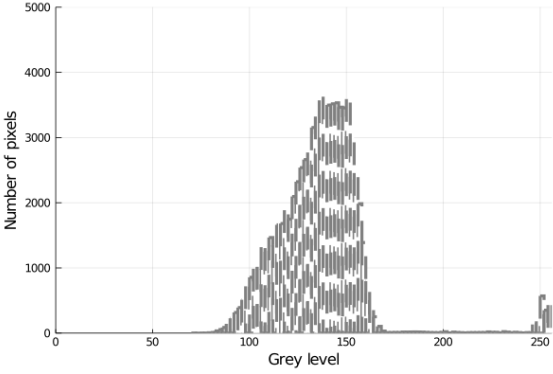
Sample	Image	Temp (°C)	Time	Histogram
CAB4		750	15 min	
		500	30 min	
		500	2 hrs	

Table 4: Optical microscope color images of the alloy microstructures after different heat treatments with respect to time for CAB4. The histograms are obtained after transformation of the pixel color of the images into grey scale images.

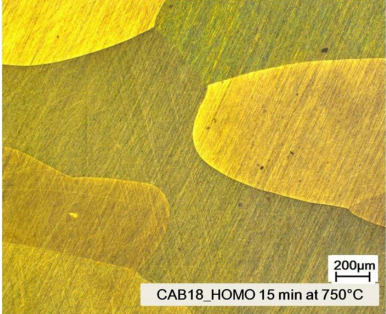
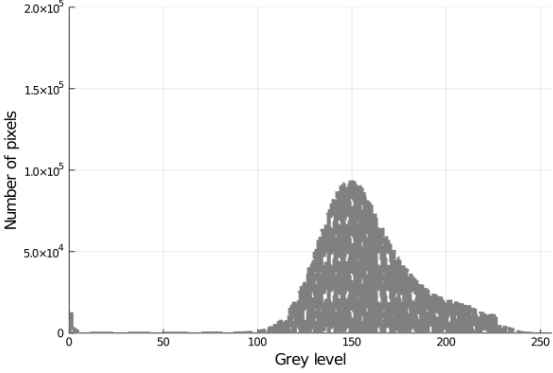
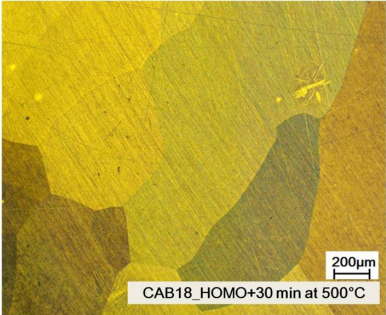
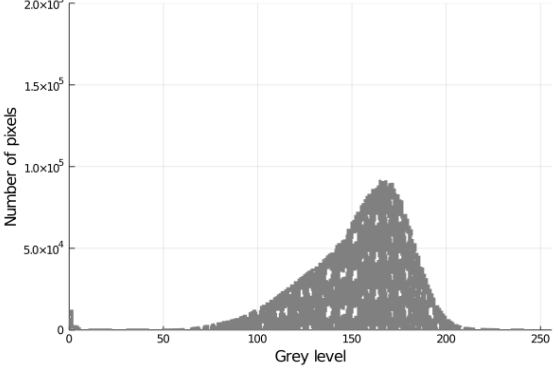
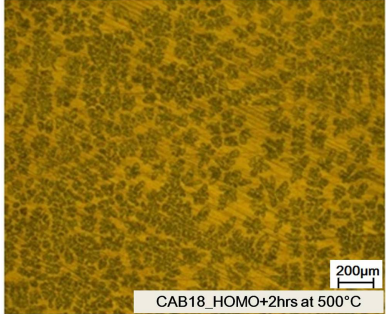
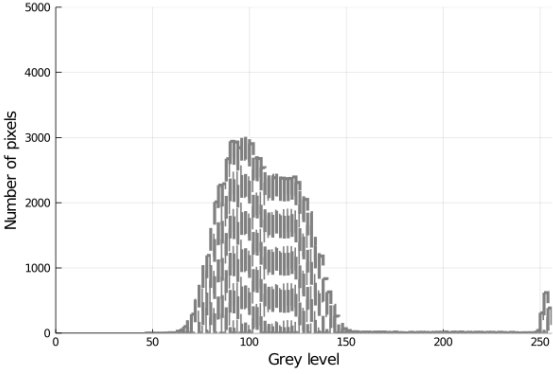
Sample	Image	Temp (°C)	Time	Histogram
CAB18		750	15 min	
		500	30 min	
		500	2 hrs	

Table 5: Optical microscope color images of the alloy microstructure after different heat treatments with respect to time for CAB18. The histograms are obtained after transformation of the pixel color of the images into grey scale images.

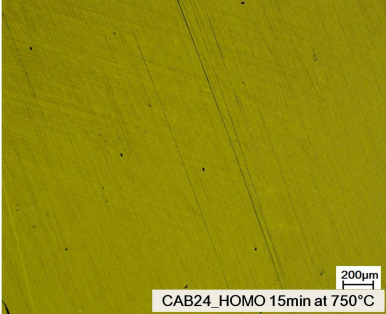
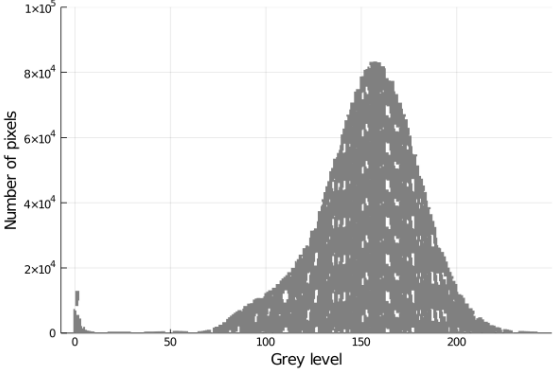
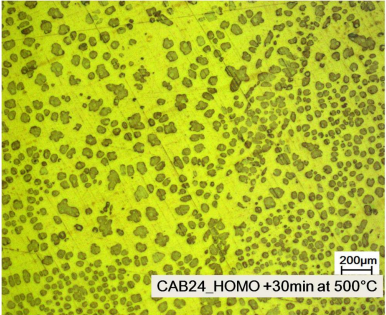
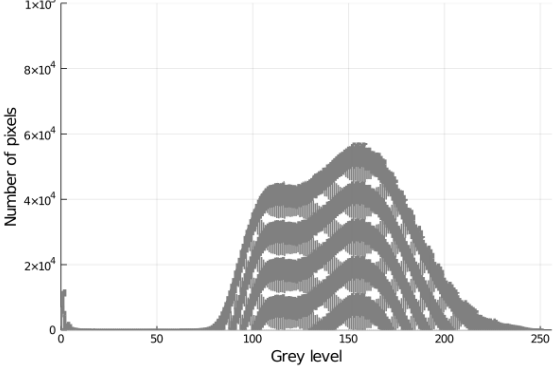
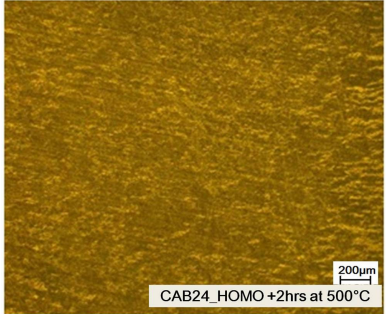
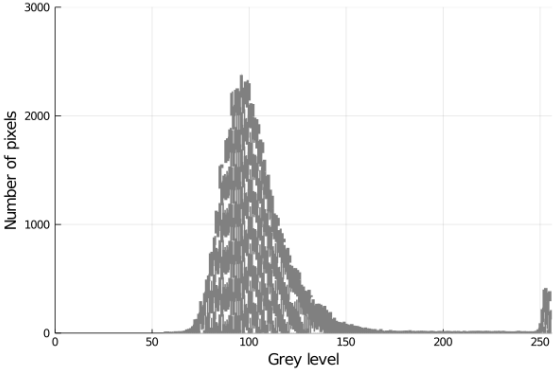
Sample	Image	Temp (°C)	Time	Histogram
CAB24		750	15 min	
		500	30 min	
		500	2 hrs	

Table 6: Optical microscope color images of the alloy microstructures after different heat treatments with respect to time for CAB24. The histograms are obtained after transformation of the pixel color of the images into grey scale images.

martensitic  $\beta'_1$  - phase , precipitate  $\gamma_1$  - phase, e.t.c. The phase Mappings were done using the EDAX TEAM™ EDS Software Suite for SEM (Ametek, Berwyn, PA, U.S.A). The indexing was performed based on the phase diagram at 500 °C for CAB4, as referenced in Belkhala’s article [4]. In this diagram, the presence of phases  $\alpha$ ,  $\beta$ , and  $\gamma_2$  was observed, providing the basis for the indexing of the alpha precipitates.

The atomic and weight percentages of the *Cu-Al* element phases at the points chosen on the SEM-EDS images and the ultrasonic wave signals reflected by the SMA samples, are depicted in Table 7. The measurement represents an average taken from multiple points within the zone. The reported composition is an outcome of comprehensive sampling across various locations within the area of interest. This approach was adopted to account for composition heterogeneity and ensure a representative assessment of the alloy’s chemical composition.

The phases of the alloys (CAB4, CAB18 and CAB24) were identified from the phase diagram in references [4, 30, 31] and the relative amounts of the determined phases (*phase composition*) calculated using the lever rule (the inverse lever rule). Therefore, these values were determined using the SEM-EDS data, a temperature of 750°C, and from the overall composition position on the tie line as depicted by a circle or a line in Fig. (5). The fraction of one phase was computed by taking the length of the tie line from the overall alloy composition to the phase boundary for the other phase, and dividing by the total length of the tie line. The phases composing the alloys were then to be binary alloys and were combinations of the  $\beta$ ,  $\gamma_1$  and  $\varepsilon_2$  phases. To ascertain the effective modulus of the phases in the SMA alloys, we initially calculated the theoretical stiffness constants for each phase using ab initio methods (DFT). The effective Young’s modulus was then the sum of the individual mass contributions of each alloy phase.

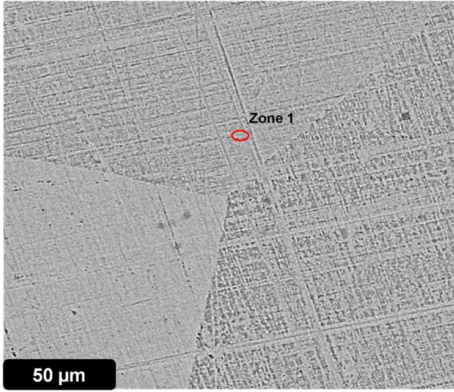
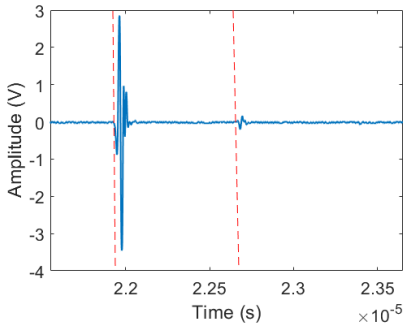
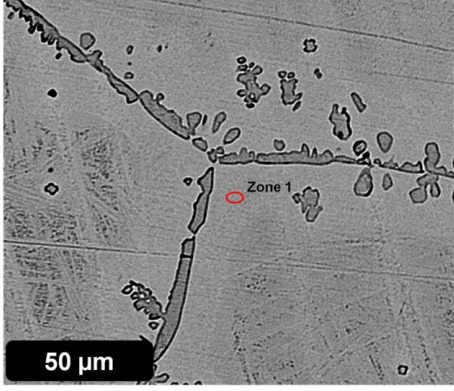
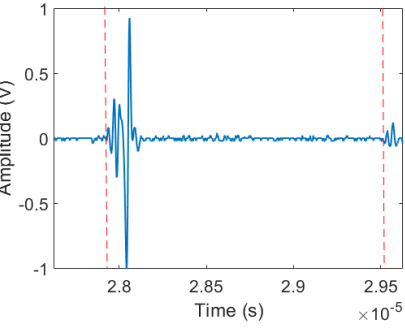
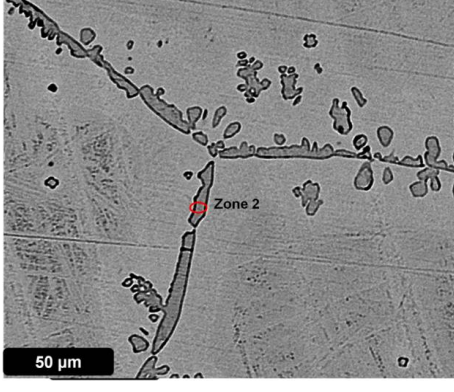

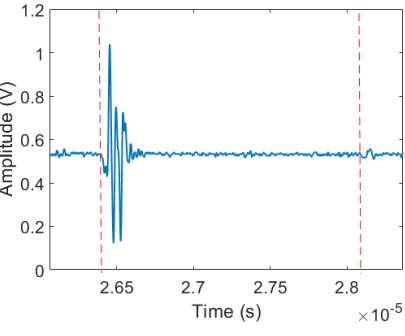
SMA	SEM	At% (Al, Cu)
Cab4 <sub>2</sub> H		 (28.57, 71.43)
Cab18 <sub>4</sub> H		 (27.30, 72.70)
Cab18 <sub>4</sub> H		 (35.30, 64.70)
Cab24 <sub>4</sub> H		 (37.71, 62.29)

Table 7: SEM images of the *Cu-Al-Be* SMAs, the phases given by the EDS analysis (region of interest - zone1) and the corresponding reflected temporal ultrasonic wave signal from which the TOF is retrieved. The second vertical line on the temporal signal plot marks the arrival of the reflected wave from the rear face of the sample.

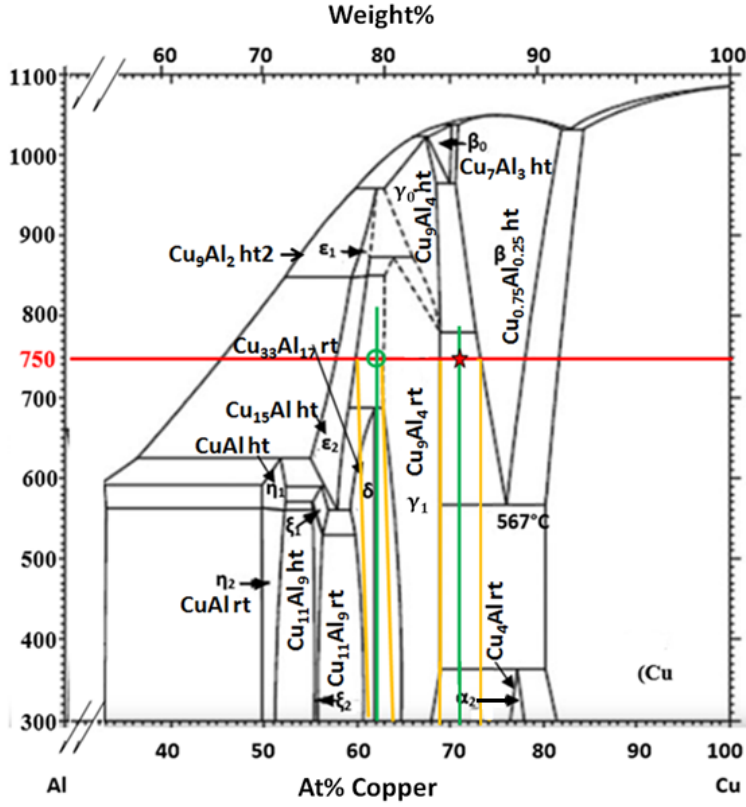


Figure 5: The  $Cu - Al$  phase diagram [4, 30, 31] showing the region of interest. Using the tie line at  $750^\circ C$ , the atomic fraction at points marked with (a)  $\circ$  is for Cab24<sub>2</sub>H SMA, (b) the  $\star$  is for Cab4<sub>2</sub>H.

For materials with a cubic lattice structure only three stiffness constants are necessary ( $c_{11}$ ,  $c_{12}$  and  $c_{44}$ ) of the 36 components  $c_{ij}$  because they are independent. From the fitting of stress against strain, these elastic stiffness constants were obtained. They are presented in Table (8). Values of the bulk (B), shear (G), and Young's modulus (E) can be calculated from these constants [32, 33]. They were calculated under the Hill scheme [34], which consists of averaging the estimates of the Reuss (lower bound) and Voigt (upper bound) methods.

The chemical composition of the identified alloys are given in Table (9). The mass fraction of each alloy in the distributions of the compositions and the global Young's moduli are also given.



Alloy phases	$c_{11}$	$c_{12}$	$c_{44}$	B	G	E	$\nu$	$\rho$ (kg/m <sup>3</sup> )	a (Å)	Space Group
$\beta$ , this work	151.0	126.0	97.0	134.0	45.0	119.0	0.353	7565	8.6388	
Ref. [35]	147.0	122.0	99.0	130.3	45.3	121.88	0.344	7270		Fm $\bar{3}$ m [225]
Ref. [8]	137.2	128.0	99.1	131.2	47.7	127.7	0.338			
Ref. [36]	137.4	108.3	95.7	126.2						
$\gamma_1$ , This work	230.0	87.0	65.0	135.0	68.0	174.0	0.285	7100		
Ref. [35]	226	81.0	68.0	129.3	69.8	177.4	0.27139	6850	8.701	P $\bar{4}$ 3m [215]
Ref. [37]									8.71	
$\varepsilon_2$ , This work				164.7	60.5	161.7	0.3358			

Table 8: Computed elastic stiffness constants (in GPa) and the corresponding elastic moduli and lattice parameters. Reference [35] is the basis method for obtaining stiffness constants values in Materials Project [38].

SMA alloy	Phases	Chem. form.	Mass fraction $\gamma_1$ ( $\Theta$ )	Ab Initio effective mixt. E(GPa)
Cab4 <sub>2</sub> H	$\beta$ & $\gamma_1$	$AlCu_3$ & $Al_4Cu_9$	0.44	98.0
Cab24 <sub>2</sub> H	$\varepsilon_2$ & $\gamma_1$	$AlCu_{15}$ & $Al_4Cu_9$	0.83	173.0
Cab18 <sub>4</sub> H	$\beta$ & $\gamma_1$	$AlCu_3$ & $Al_4Cu_9$	0.26	74.8
Alum.	$Al$	$Al$	-	(E=69, $\nu$ =0.364)

Table 9: The identified phases from the SEM with EDS analysis of the homogenized SMAs, their chemical formulae (Chem. form.). The Young's modulus is calculated using  $E_{effective} = \Theta E_{phase\gamma_1} + (1-\Theta)E_{phase2}$ . Aluminium is also given for comparison.

#### 4.4. Using the ultrasonic vibration spectroscopy data to verify the retrieved parameters

The calculated Young's modulus was recovered using the SEM-EDS analysis and the phase diagram (values in Table 9) were used to compute the vibrational frequency response of the SMA alloy samples ([11]) using 3D FEM steady state dynamic response analysis. The responses are depicted in Fig. (6). The peaks coincide for the lower modes and also for some very high modes. Some peaks in the experimental data are absent in the computed spectra, this maybe due to the direction of excitation and the point where the measurements are made on the sample. The good agreement shows that the method of mixtures with the lever rule method applied to the phase diagram are precise, if the diagram is accurate. The discrepancies can come from the precise identification of the atomic weight percentages on the diagram. The adjustment of the  $E_{effective}$  can be done in order to make the resonance peaks to better coincide. In the case of Cab4<sub>2</sub>H the calculated value was 98 GPa but adjusting this value to 91 GPa improved the coincidence of the experimental and theoretical resonance peaks.

#### 4.5. Ultrasonic Time-of-Flight Measurements in Water-Immersed Sample Layers

The times of flight for the reflected signals were obtained from both the temporal reflected peaks and the scalogram, as shown in Fig. (7). Using the measured thickness of the sample and the time difference between the specularly reflected wave and the wave that travels to and fro and reflects at the back surface of the sample, we calculated the wave velocity within the sample layer [26]. To determine the mass densities, we weighed the sample using an electronic balance and calculated its volume from its measured geometry.

The retrieved values of the TOF, the wave velocities and the P-Wave modulus for the different homogenized *Cu-Al-Be* SMA samples are shown in Table (10).

The experimentally retrieved TOF and P-wave moduli for the heat treated *Cu-Al-Be* SMA samples are listed in Table (11).

The experimental data presented in Table (10) and Table (11) provide valuable insights into the P-wave modulus variations with temperature in the homogenized *Cu-Al-Be* SMA samples. The increase in P-wave modulus after heat treatment can be attributed to the presence of specific phases, namely  $\gamma_1$  and  $\varepsilon_2$ , in the mixtures, as indicated by the

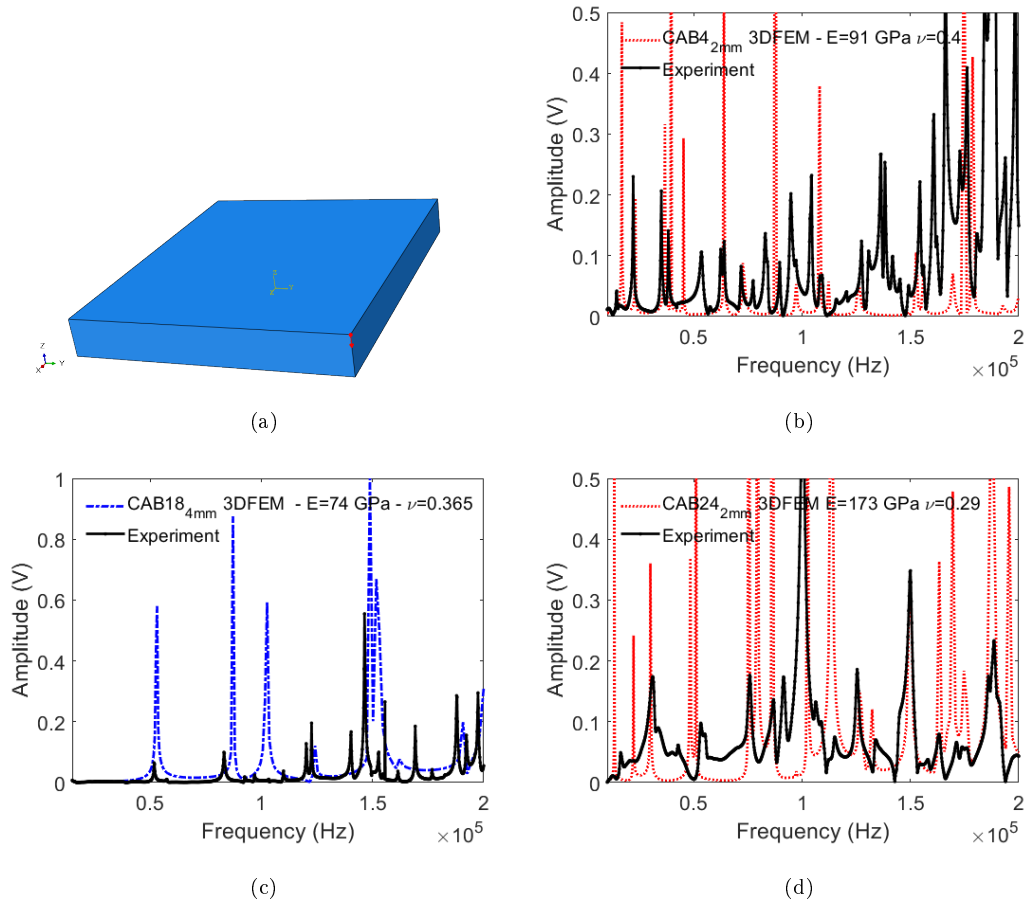


Figure 6: Comparison between the steady state vibrational spectroscopy experimental response and the 3D FEM steady state computed response of the SMA alloys. (a) The geometry of CAB4, (b) vibration spectrum for Cab4<sub>2</sub>H (c) Cab18<sub>4</sub>H (d) Cab24<sub>2</sub>H. The force was applied at the corner and at the edges for the circular samples.

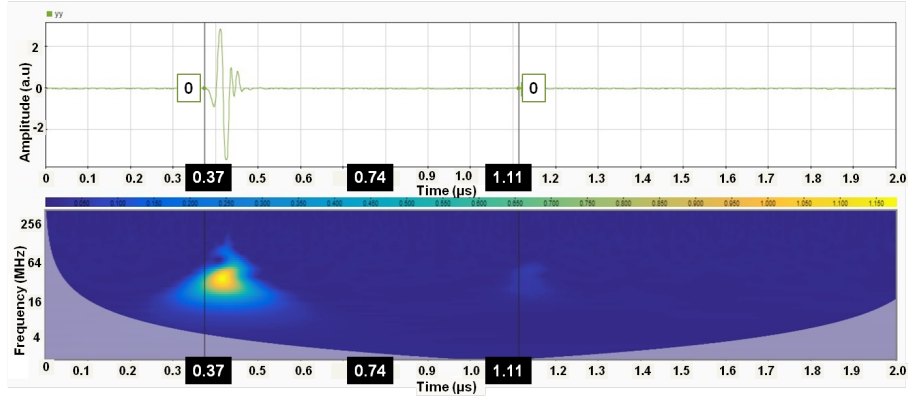


Figure 7: Upper panel: Temporal signal of an ultrasonic wave reflected by sample CAB4<sub>2</sub>H immersed in a water tank. The time of flight (TOF) is obtained by measuring the time difference between the reflection on the first surface facing the transducer and the reflection on the back surface within the sample. Lower panel: Time-frequency scalogram of the temporal signal. The first reflection on the surface of the sample is indicated by the start cursor, and the reflection on the back surface is indicated by the stop cursor. The TOF is calculated as the difference between the two, here a duration of 0.74  $\mu\text{s}$ .

SMA	thickness (mm)	density ( $\text{kg}/\text{m}^3$ )	TOF ( $\mu\text{s}$ )	$V$ (m/s)	$M_{us} = \rho_s V^2$ (GPa)
Cab4 <sub>2</sub> H	2.0	7200	0.75	5333	204.8
Cab4 <sub>3</sub> H	3.0	7200	1.15	5217	196.0
CAB24 <sub>4</sub> H	4.0	7264	1.68	4762	163.3
CAB24 <sub>2</sub> H	2.0	7068	0.88	4545	144.63
CAB18 <sub>4</sub> H	4.0	7094	1.58	5063	182.0

Table 10: Results for the homogenized SMA *Cu-Al-Be* samples (15 minutes heating at 750 °C): the TOF, ultrasonic wave velocities ( $V$ ), P-wave moduli ( $M_{us}$ ), Young's modulus and Poisson ratio obtained from ultrasonic vibration experiment.

SMA	thickness (mm)	density (kg/m <sup>3</sup> )	TOF ( $\mu$ s)	velocity (m/s)	M (GPa)
Cab4 <sub>2</sub> H+30 @500°C	2.0	7200	0.73	5480	216
CAB24 <sub>2</sub> H+30 @500°C	2.0	7075	0.78	5128	186
CAB18 <sub>4</sub> H+30 @500°C	4.0	7094	1.588	5038	180

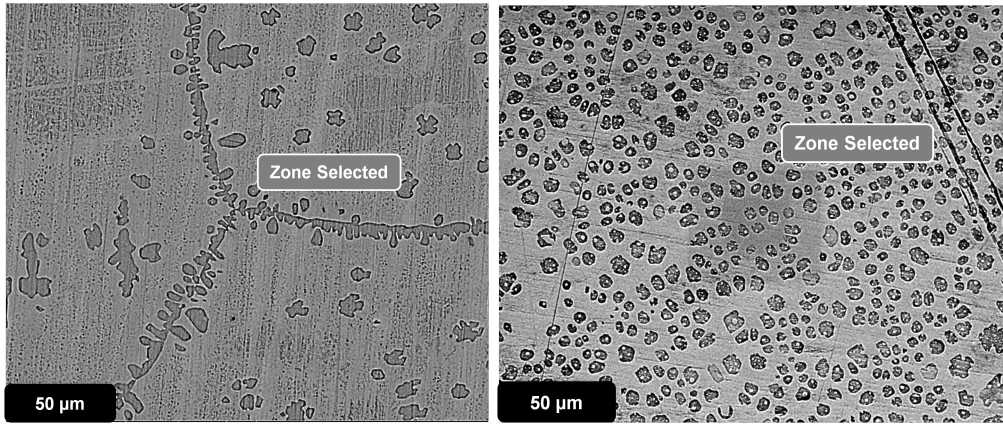
Table 11: The TOF, wave velocities and P-wave modulus for the homogenized samples (annealing heat treatment for 30 minutes at 500 °C).

phase diagram (Fig. 5). These phases have distinct mechanical properties, influencing the overall stiffness of the material.

Regarding the P-wave modulus, a comprehensive analysis of the data along with temperature variations can provide further insights. Comparing the P-wave modulus values at different temperatures allows for the study of the material’s compressibility under varying thermal conditions. Additionally, examining the variations in P-wave modulus across different phases and compositions, especially in the presence of heat treatment, can elucidate the impact of thermal processes on the material’s elastic properties.

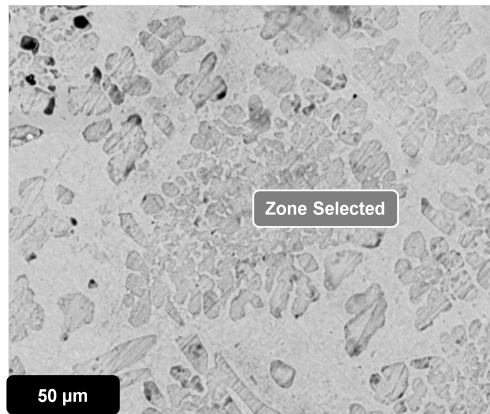
Further experiments and analysis could involve systematically varying the temperature and conducting detailed measurements of P-wave modulus and Young’s modulus for different phases and compositions within the *Cu-Al-Be* SMA system. This systematic approach would provide a more comprehensive understanding of the material’s behavior under different thermal treatments and enable the establishment of a clearer relationship between bulk modulus, Young’s modulus, and temperature.

Figure (8) displays scanning electron microscope images of CAB4, CAB24, and CAB18 samples subjected to a 15-minute homogenization treatment at 750°C, followed by a 30-minute treatment at 500°C. After the 500°C treatment, the emergence of precipitates can be observed in comparison to the images in Table (7) (depicting samples that underwent only a 15-minute homogenization treatment at 750°C). The emergence of these precipitates, observed in Figure (8), correlates with the increased velocities and the P-wave modulus (M), as indicated by a comparison between the values in Table (11) and Table (10). However, CAB18 exhibited precipitates both before and after the 500°C treatment, indicating that the homogenization treatment was insufficient to eliminate all remaining precipitates from previous processes.



(a)

(b)



(c)

Figure 8: SEM images with EDS analysis after heat treatment of the SMA samples. The samples underwent a 15-minute homogenization treatment at 750 °C, followed by a 30-minute treatment at 500 °C. Compositions taken at the labeled points in the *zone* are provided in atomic percentage (At %) for (*Al*, *Cu*). (a) CAB4: (34.18%, 65.82%), (b) CAB24: (32.51%, 67.49%), (c) CAB18: (35.30%, 64.70%).

## 5. Discussion

### 5.1. Relating the P-wave modulus $M$ obtained from the tank experiment with the effective Young's modulus ( $E_{effective}$ ) and the UVS experiment

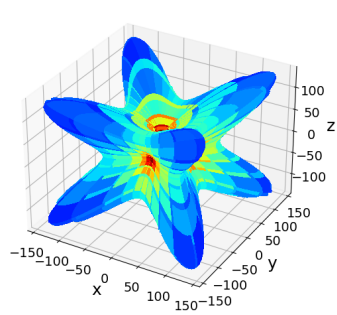
The relationship in Eqn. (2) (function of the Young's modulus and Poisson's ratio), is employed to relate the water tank experiment  $M$  values to those obtained using  $E$  vibration. As an example, the  $E_{effective}$  and  $M_{us}$  for CAB18<sub>4</sub>H are 74 GPa and 189 GPa respectively. For the two moduli to be equivalent (Eqn. (2), the Poisson ratio should be  $\nu = 0.419$ . For CAB4<sub>2</sub>H,  $\nu = 0.406$ .

In the case where  $E_{effective}$  is greater than  $M_{us}$  (P-wave modulus) for the material CAB24<sub>2</sub>H, it results in an effective Young's modulus that exceeds  $M_{us}$ . When using Equation (2) to relate  $M$  and  $E_{effective}$ , it implies that the calculated Poisson ratio falls outside the typical range, i.e.,  $(-\infty, -1)$  and  $(1/2, \infty)$ .

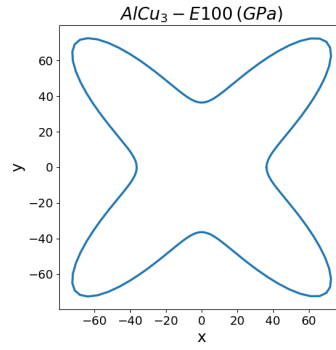
### 5.2. The Spatial dependence of Young's modulus

The samples were in the form of cylinders, and their main crystallographic direction was (100). This is the direction in which measurements were conducted on the samples. These cylinders were fabricated using the Bridgman method [39, 20] and were subsequently cut into small discs with a thickness ranging from 2 to 4 mm using a cold saw.

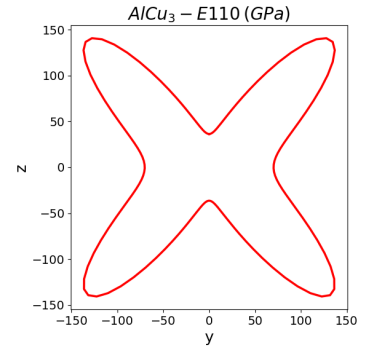
The Spatial dependence of the Young's modulus curves for the  $\beta$  and  $\gamma$  phases of the SMA are plotted in Fig. (9) using techniques described in [32, 33]. They both have cubic lattice structures. The  $\beta$  phase's Young's modulus dependence on the spatial direction in the  $(xy)$  plane, also known as  $E_{100}$ , can explain the lower experimental values found for CAB18<sub>4</sub>H ( $\approx 74$  GPa), see Fig. 9b. The lower values at 40 GPa found in other studies like the one using a non-destructive impulse excitation technique [13] can be explained by this directional spatial variation of Young's modulus as highlighted herein.



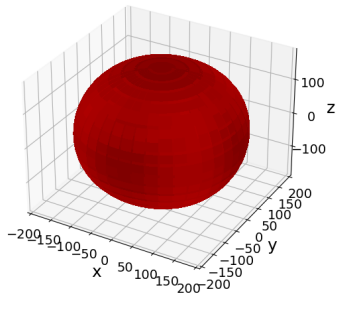
(a)



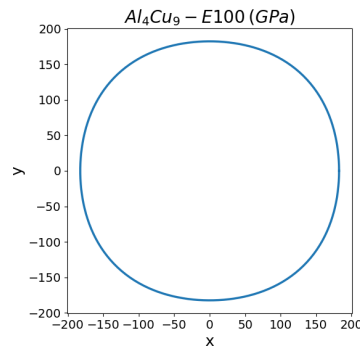
(b)



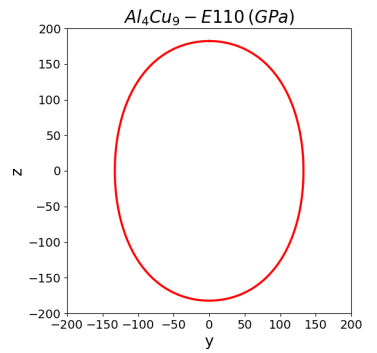
(c)



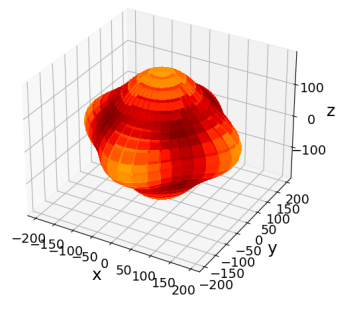
(d)



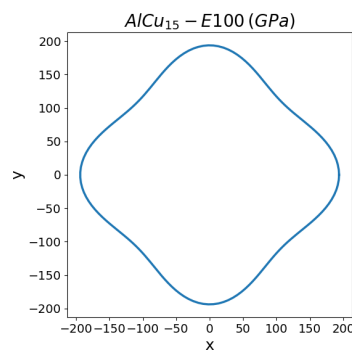
(e)



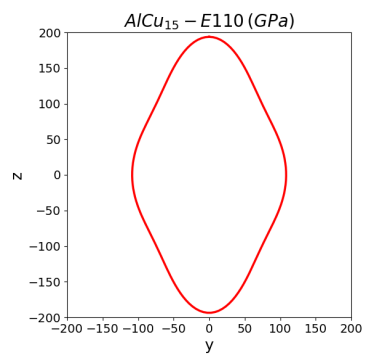
(f)



(g)



(h)



(i)

Figure 9: The spatial dependence of Young's modulus (GPa) for the  $\beta$  (a, b, c),  $\gamma$  (d, e, f) and  $\epsilon_2$  (g, h, i) phases of the SMAs.



## 6. Analysis of the composition of the SMAs by comparing the X-ray diffraction patterns from measurements with those retrieved from computed phase diagrams and the respective EDS data

X-ray diffraction patterns were obtained for the SMAs using  $\text{CuK}\alpha$  radiation with a wavelength of 1.542 Å. To identify the intermetallic alloy phases present in each SMA, the EDS concentrations and temperature (750° C) were cross-referenced with the computed phase diagram using Thermo-Calc software [40]. The identified phases are listed in Table A.12. Theoretical powder X-ray patterns were then computed for these identified phases using Vesta software [41] and compared to the measured diffraction patterns. Notably, it should be mentioned that while there may be differences between diffraction patterns obtained from powder and single crystals, both methods offer valuable insights into the crystal structure of the material.

For the SMA CAB<sub>42</sub>H, EDS analysis revealed a composition of 14.37 wt% aluminum and 85.63 wt% copper after a 15-minute homogenization treatment at 750° C. Analysis of the DRX diffractogram patterns (see Fig. A.10a) indicated the presence of several phases. The  $\beta$  austenitic phase ( $\text{AlCu}_3$  with a cubic  $\text{Fm}\bar{3}\text{m}$  crystal structure) was detected, along with precipitates of  $\gamma$  ( $\text{Al}_4\text{Cu}_9$  with a gamma-brass-like structure in cubic  $\text{P}\bar{4}3\text{m}$  space group), which were remnants from the previous treatment at 500° C. This suggests that the homogenization treatment was not sufficient to eliminate all the precipitates. Additionally, the presence of copper was observed due to the stabilization of the austenitic phase, which caused the blocking of the sample. These findings confirm the previous analysis results. The semiquantitative percentage (SQP) values for  $\beta$  and  $\gamma$  phases are provided in Table (A.12). The Young's modulus for CAB<sub>42</sub>H was calculated using the rule of mixtures, SQPs, and considering the directional modulus, resulting in a value of 101 GPa (compared to 91 GPa from the VS experiment - FEM, as shown in Fig. 6b).

In Fig. A.10b, the alloy was subjected to a homogenization treatment followed by annealing at 500° C. The diffractogram shows the presence of the austenitic phase and precipitates  $\gamma$  and  $\text{Al}_3\text{Cu}_2$ .

After the homogenization treatment of the CAB<sub>184</sub>H alloy (composition of 13.76 wt% Al, 86.24 wt% Cu), the DRX diffractograms, the sample mainly consisted of the  $\beta$  and  $\gamma$  phase

### 6.1. *Exploring the Relationship Between Volume Fraction of Precipitates and Young's Modulus*

The influence of grain size on the pseudoelastic behavior of Cu-Al-Be alloys has been studied by Montecinos et al. [42]. Their research demonstrated that grain size significantly affects the material's response during the martensitic transformation. Specifically, larger grain sizes were found to be associated with reduced martensite-start stress and modified strain retention characteristics. This indicates that the size of the grains plays a crucial role in determining the mechanical properties and behavior of Cu-Al-Be alloys.

To address potential limitations associated with grain size (not a limitation in the present study), several approaches can be considered. One of them is increasing the sample size so as to incorporate a larger number of grains, improving the statistical reliability of the data. This can be achieved by fabricating larger specimens or by collecting data from multiple smaller samples to increase the overall grain count.

Another approach is to carefully select the sample orientation and cutting planes. By choosing appropriate orientations and cutting planes, it is possible to maximize the number of grains observed and analyzed within the sample. This can provide a more representative understanding of the material's properties, accounting for the anisotropic nature of the grain structure.

Overall, addressing limitations associated with grain size involves careful sample selection, consideration of orientation and cutting planes, and potentially utilizing advanced techniques like electron backscatter diffraction (EBSD). These strategies can help mitigate the limitations and improve the accuracy of the analysis of SMAs with respect to grain size.

The maximum and minimum values of the Young's modulus in the E100 direction for the  $\beta$  phase (Fig. 9) are  $\approx 70$  GPa and  $\approx 20$  GPa respectively. The higher the percentage of  $\gamma$  precipitates, the higher will be the value of Young's modulus of the mixture  $\beta + \gamma$ . The  $\gamma$  phase being quasi-isotropic and its Young's modulus (170 GPa) is approximately more than twice that of the  $\beta$  phase, its contribution to the mixture is more significant. If the rule of mixtures is considered [17], the effective value will greatly increase if the quantity of the precipitates increase. The effective Young's modulus of the composite ( $E_c$ ) is given by the rule of mixtures

$$E_C = fE_\gamma + (1 - f)E_\beta,$$

where  $f$  is the volume fraction and  $E_\gamma$  is the Young's modulus of the  $\gamma$  phase,  $E_\beta$  is that of the  $\beta$  phase. The fraction  $f$  can be retrieved from the histogram representing the analysis of the SEM gray scale color image [43, 44].

### 6.2. The elements at the grain boundary

The analysis of the SEM-EDS data revealed the atomic composition of (Al, Cu) at the boundary joints in CAB18<sub>4</sub>H to be (at% 35.30, at% 64.70) (Table 7). This composition corresponds to the presence of the  $\varepsilon_2$  and  $\gamma$  phases as predicted by the phase diagram.

In summary, the analysis of the grain boundary composition in CAB18<sub>4</sub>H revealed the presence of the  $\varepsilon_2$  and  $\gamma$  phases. The study by Montecinos et al. highlighted the importance of grain size in influencing the pseudoelastic behavior of Cu-Al-Be alloys. These findings emphasize the significance of grain characteristics in determining the mechanical response and properties of shape memory alloys, providing valuable insights for further research and engineering applications.

## 7. Conclusion

The transformation points of the shape memory alloys were determined by measuring and analyzing the peaks of heat generation and absorption using differential scanning calorimetry. A metallography analysis using an optical microscope was also undertaken to identify the nature and grain size of the alloy phases present in the samples after different heat treatments.

This study introduced a novel method for determining the effective Young's modulus of SMAs. By utilizing SEM-EDS data, phase diagrams, and the inverse lever rule method, the fractional mass percentage of each phase in the SMAs was determined. These findings, in conjunction with the Young's modulus calculated from the Ab Initio DFT method for each phase, allowed for the computation of the effective Young's modulus ( $E_{effective}$ ). Notably, new elastic constants data were generated for the  $\varepsilon_2$  phase. The analysis revealed that the  $\beta$  phase exhibited highly anisotropic Young's modulus, with  $E_{100}$  values ranging from 40 GPa to 70 GPa. These findings provide insights into the

previously observed lower Young's modulus values reported in the literature for *Cu-Al-Be* SMAs. The comprehensive utilization of SEM-EDS, phase diagrams, and theoretical X-ray diffraction patterns ensured the precise identification of phases within the SMAs, establishing a solid foundation for further investigations into their unique properties and potential applications.

Characterizing small-sized, flat SMA samples can be challenging due to their size and shape. To overcome this challenge, the samples were probed using high-frequency (50 MHz) ultrasonic bulk waves that propagate within the layer thickness. Specifically, the wave velocity measurements were determined by calculating the time of flight difference between the wave reflected from the front and the back-face of the sample layer, having travelled within it. By using this approach, an accurate measurement of the wave velocity within the sample was obtained, which provided valuable information about the material's properties. This technique was crucial for characterizing the SMAs used in this study, as it allowed the authors to obtain important data for subsequent analyses and modeling.

The computed peaks of the resonance frequencies in the vibration spectrum were found to agree well with those obtained from the ultrasonic vibration spectroscopy experiment, providing validation. The P-wave modulus was then related to the effective Young's modulus, which was confirmed by both the mechanical vibration spectroscopy experiments and the 3D FEM analysis of the SMA alloy samples. It was found that a value of Poisson ratio  $\nu, \approx, 0.41 \dots$  was required to associate the P-wave modulus with the effective Young's modulus, except for the CAB24<sub>2</sub>H alloy. After heat treatment of the SMA samples, the P-wave modulus increased, along with the wave speed.

## **Appendix A. Comparison of X-ray diffraction patterns**

To validate the identified phases, X-ray diffraction patterns were measured and compared with those computed based on the data obtained from the phase diagram. The X-ray diffraction patterns were calculated using Vesta software [41], while the intermetallic alloy phases were obtained from computed phase diagrams using Thermo-Calc software [40]. In addition, the concentrations of the elements were determined from experimental data presented in Table 7. By combining these techniques, a thorough

characterization of the phases present in the SMAs was achieved, which was essential for subsequent analyses and modeling of the materials' properties.

SMA	Wt%(Al, Cu)	Phase T-C	Symbol	XRD-Experiment		
				Space group	Number	Lattice
$CAB_4H$	(14.37, 85.63)	BCC_β2	$\beta-AlCu_3$	$Fm\bar{3}m$	225	cubic
		GAMMA_D83	$\gamma-Al_4Cu_9$	$P\bar{3}m$	215	cubic
$CAB_{18}H$	(13.76, 86.24)	BCC_β2	$\beta-AlCu_3$	$P6_3/mmc$	194	hexagonal
		GAMMA_D83	$\gamma-Al_4Cu_9$	$P\bar{3}m$	215	cubic
			$\theta-Al_2Cu$ (C16)	$I4/mcm$	140	tetragonal
$CAB_{24}H$	(20.45, 79.55)	ALCU_EPS	$\theta-Al_2Cu$ (C16)	$I4/mcm$	140	tetragonal
		GAMMA_D83	$\gamma-Al_4Cu_9$	$P\bar{3}m$	215	cubic

Table A.12: Retrieved phases from the matching of the x-ray diffraction patterns with the measured ones for the homogenized SMA (15-minute homogenization treatment at 750 °C).

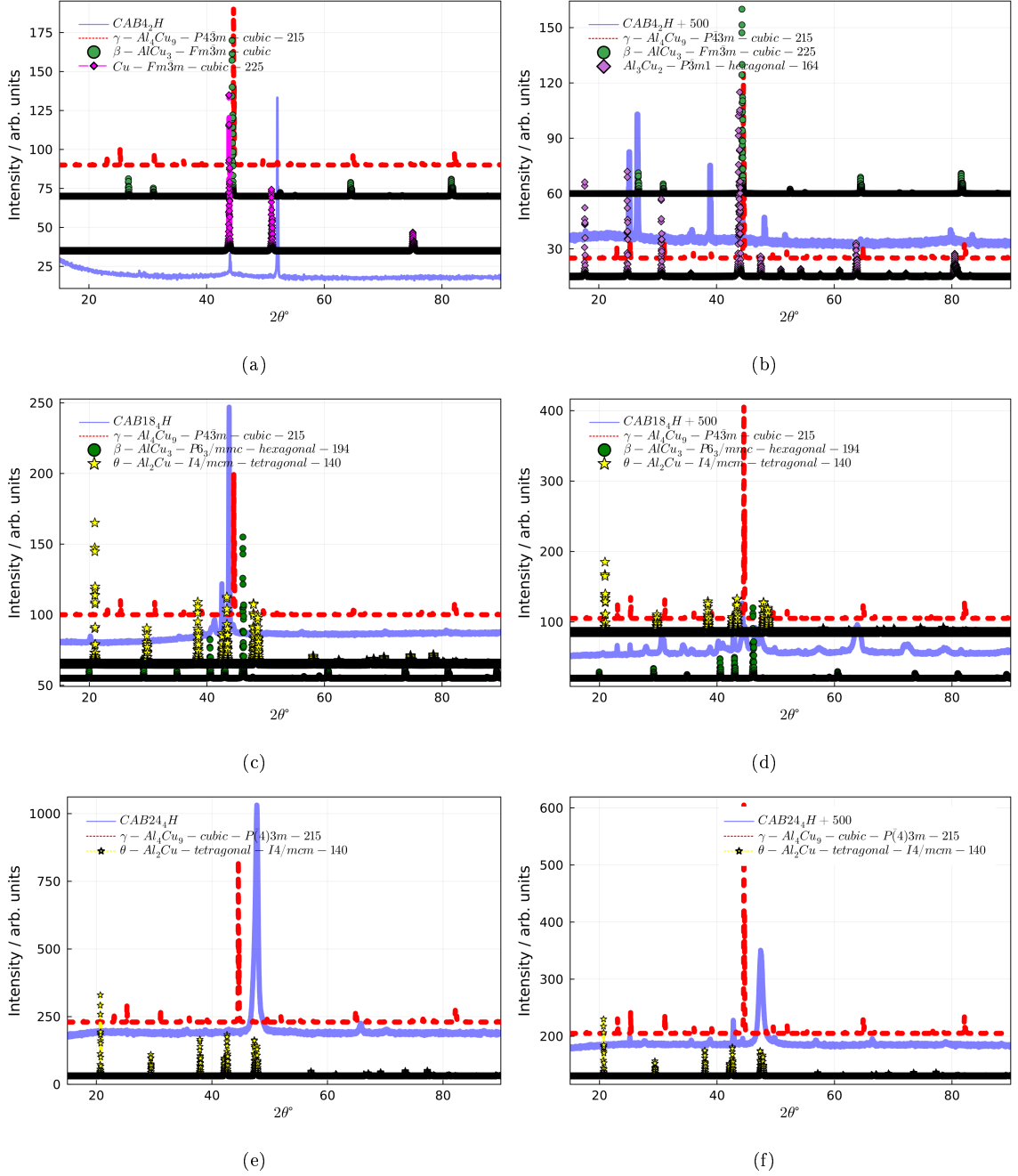


Figure A.10: The computed x-ray diffraction patterns were matched with the measured ones in order to identify the phases present in the shape memory alloys (15-minute homogenization treatment at 750 °C, followed by a 30-minute treatment at 500 °C) (a)  $CAB_4H$  (b)  $CAB_4H+500$  (c)  $CAB_{18}H$  (d)  $Cab_{18}H+500$  (e)  $Cab_{24}H$  (f)  $Cab_{18}H+500$ .

## References

- [1] A. Planes, L. M. nosa, Vibrational properties of shape-memory alloys (2001).  
URL <https://www.sciencedirect.com/science/article/pii/S0081194701800059>
- [2] E. C. Pereira, L. A. Matlakhova, A. N. Matlakhov, C. J. de Araújo, C. Y. Shigue, S. N. Monteiro, Reversible martensite transformations in thermal cycled polycrystalline Cu-13.7%Al-4.0%Ni alloy, *Journal of Alloys and Compounds* 688 (2016) 436–446.  
URL <https://www.sciencedirect.com/science/article/pii/S0925838816322459>
- [3] H. Sehitoglu, X. Y. Zhang, Y. I. Chumlyakov, I. Karaman, K. Gall, H. J. Maier, Observations on stress-induced transformations in niti alloys, in: Q. P. Sun (Ed.), *IUTAM Symposium on Mechanics of Martensitic Phase Transformation in Solids*, Springer Netherlands, Dordrecht, 2002, pp. 103–109.
- [4] S. Belkahla, *Elaboration et caractérisation de nouveaux alliages à mémoire de forme basse température type cualbe*, Ph.D. thesis, INSA, Lyon, France (1990).
- [5] V. H. C. de Albuquerque, T. A. de A. Melo, R. M. Gomes, S. J. G. de Lima, J. M. R. Tavares, Grain size and temperature influence on the toughness of a CuAlBe shape memory alloy, *Materials Science and Engineering: A* 528 (1) (2010) 459 – 466, special Topic Section: Local and Near Surface Structure from Diffraction.  
URL <http://www.sciencedirect.com/science/article/pii/S0921509310010646>
- [6] S. Belkahla, H. Flores Zuñiga, G. Guenin, Elaboration and characterization of new low temperature shape memory Cu-Al-Be alloys, *Materials Science and Engineering A* 169 (1) (1993) 119 – 124.  
URL <http://www.sciencedirect.com/science/article/pii/092150939390606F>
- [7] H. Kuo, W. Wang, Y. Hsu, Microstructural characterization of precipitates in Cu10wt.%Al-0.8wt.%Be shape-memory alloy, *Materials Science and Engineering: A* 430 (1) (2006) 292 – 300.  
URL <http://www.sciencedirect.com/science/article/pii/S0921509306008768>
- [8] A. Alés, Study of different structures derives of  $\beta$ -Cu3Al by means of ab-initio calculations and quasi-harmonic approximation, *Computational Condensed Matter* 31 (2022) e00652.  
URL <https://www.sciencedirect.com/science/article/pii/S2352214322000132>
- [9] A. Jain, S. P. Ong, G. Hautier, W. Chen, W. D. Richards, S. Dacek, S. Cholia, D. Gunter, D. Skinner, G. Ceder, K. a. Persson, The Materials Project: A materials genome approach to accelerating materials innovation, *APL Materials* 1 (1) (2013) 011002.  
URL <http://link.aip.org/link/AMPADS/v1/i1/p011002/s1&Agg=doi>
- [10] E. Ogam, A. Wirgin, S. Schneider, Z. Fella, Y. Xu, Recovery of elastic parameters of cellular materials by inversion of vibrational data, *J. Sound Vibr.* 313 (3-5) (2008) 525–543.
- [11] D. Chanbi, E. Ogam, S. E. Amara, Z. E. Fella, Synthesis and mechanical characterization of binary and ternary intermetallic alloys based on Fe-Ti-Al by resonant ultrasound vibrational methods, *Materials* 11 (5) (2018) 746.
- [12] D. A. Porter, K. E. Easterling, *Phase Transformations in Metals and Alloys*, 2nd Edition, CRC Press, 1992.
- [13] S. Montecinos, S. Tognana, W. Salgueiro, Determination of the young’s modulus in CuAlBe shape memory alloys with different microstructures by impulse excitation technique, *Materials Science*

- and Engineering: A 676 (2016) 121 – 127.  
 URL <http://www.sciencedirect.com/science/article/pii/S0921509316310267>
- [14] V. Recarte, M. N. J.I. J.I. Pérez-Landazábal a, J. San Juan, Study by resonant ultrasound spectroscopy of the elastic constants of the  $\beta$  phase in Cu-Al-Ni shape memory alloys, Materials Science and Engineering: A 370 (1) (2004) 488–491, 13th International Conference on Internal Friction and Ultrasonic Attenuation in Solids.  
 URL <https://www.sciencedirect.com/science/article/pii/S0921509303008372>
- [15] J. Yang, P. Ouyang, T. Liu, H. Yun, W. Sun, Y. Wang, J. Liu, S. Zhang, First-principles study of the effect of aluminum content on the elastic properties of Cu-Al alloys, Materials Today Communications 31 (2022) 103399.  
 URL <https://www.sciencedirect.com/science/article/pii/S2352492822002690>
- [16] K. N. Kudin, G. E. Scuseria, Linear-scaling density-functional theory with gaussian orbitals and periodic boundary conditions: Efficient evaluation of energy and forces via the fast multipole method, Phys. Rev. B 61 (2000) 16440–16453.  
 URL <https://link.aps.org/doi/10.1103/PhysRevB.61.16440>
- [17] N. O. Ongwen, E. Ogam, H. O. Otunga, Ab initio study of elastic properties of orthorhombic cadmium stannate as a substrate for the manufacture of mems devices, Materials Today Communications 26 (2021) 101822.  
 URL <https://www.sciencedirect.com/science/article/pii/S2352492820328336>
- [18] G. Ogam, J.-P. Groby, E. Ogam, A non-linear vibration spectroscopy model for structures with closed cracks, International Journal of Non-Linear Mechanics 59 (0) (2014) 60 – 68.
- [19] S. Belkahla, H. F. Z. niga, G. Guénin, Elaboration and characterization of new low temperature shape memory Cu-Al-Be alloys, Materials Science and Engineering: A 169 (1993) 119–124.
- [20] P. W. Bridgman, Certain physical properties of single crystals of tungsten, antimony, bismuth, tellurium, cadmium, zinc, and tin, in: Papers 32-58, Harvard University Press, 1964, pp. 1851–1932.
- [21] W. J. Boettinger, U. R. Kattner, K.-W. Moon, J. H. Perepezko, Chapter five - DTA and heat-flux DSC measurements of alloy melting and freezing, in: J.-C. Zhao (Ed.), Methods for Phase Diagram Determination, Elsevier Science Ltd, Oxford, 2007, pp. 151–221.  
 URL <https://www.sciencedirect.com/science/article/pii/B9780080446295500057>
- [22] E. Iervolino, A. van Herwaarden, F. van Herwaarden, E. van de Kerkhof, P. van Grinsven, A. Leenaers, V. Mathot, P. Sarro, Temperature calibration and electrical characterization of the differential scanning calorimeter chip ufs1 for the mettler-toledo flash dsc 1, Thermochimica Acta 522 (1) (2011) 53–59, special Issue: Interplay between Nucleation, Crystallization, and the Glass Transition.  
 URL <https://www.sciencedirect.com/science/article/pii/S0040603111000451>
- [23] M. Smith, ABAQUS/Standard User's Manual, Version 6.9, Dassault Systèmes Simulia Corp, United States, 2009.
- [24] G. Ogam, J.-P. Groby, E. Ogam, A non-linear vibration spectroscopy model for structures with



- closed cracks, *International Journal of Non-Linear Mechanics* 59 (2014) 60–68.  
 URL <https://www.sciencedirect.com/science/article/pii/S0020746213002084>
- [25] T. J. R. Hughes, *Finite Element Method - Linear Static and Dynamic Finite Element Analysis*, Prentice-Hall, Englewood Cliffs, 2000.
- [26] H. Lazri, E. Ogam, B. Amar, Z. Fellah, A. O. Oduor, P. Baki, Identification of the mechanical moduli of flexible thermoplastic thin films using reflected ultrasonic waves: Inverse problem, *Ultrasonics* 81 (2017) 10–22.  
 URL <https://www.sciencedirect.com/science/article/pii/S0041624X17304511>
- [27] P. Giannozzi, O. Andreussi, T. Brumme, O. Bunau, M. B. Nardelli, M. Calandra, R. Car, C. Cavazzoni, D. Ceresoli, M. Cococcioni, N. Colonna, I. Carnimeo, A. D. Corso, S. de Gironcoli, P. Delugas, R. A. DiStasio, A. Ferretti, A. Floris, G. Fratesi, G. Fugallo, R. Gebauer, U. Gerstmann, F. Giustino, T. Gorni, J. Jia, M. Kawamura, H.-Y. Ko, A. Kokalj, E. Küçükbenli, M. Lazzeri, M. Marsili, N. Marzari, F. Mauri, N. L. Nguyen, H.-V. Nguyen, A. O. de-la Roza, L. Paulatto, S. Poncè, D. Rocca, R. Sabatini, B. Santra, M. Schlipf, A. P. Seitsonen, A. Smogunov, I. Timrov, T. Thonhauser, P. Umari, N. Vast, X. Wu, S. Baroni, Advanced capabilities for materials modelling with quantum ESPRESSO, *Journal of Physics: Condensed Matter* 29 (46) (2017) 465901.  
 URL <https://doi.org/10.1088/1361-648x/aa8f79>
- [28] R. Hill, Elastic properties of reinforced solids: Some theoretical principles, *Journal of the Mechanics and Physics of Solids* 11 (5) (1963) 357–372.  
 URL <https://www.sciencedirect.com/science/article/pii/002250966390036X>
- [29] P. Ravindran, L. Fast, P. A. Korzhavyi, B. Johansson, J. Wills, O. Eriksson, Density functional theory for calculation of elastic properties of orthorhombic crystals: Application to tisi<sub>2</sub>, *Journal of Applied Physics* 84 (9) (1998) 4891–4904.  
 URL <https://doi.org/10.1063/1.368733>
- [30] P. Kah, C. Vimalraj, J. Martikainen, R. Suoranta, Factors influencing Al-Cu weld properties by intermetallic compound formation, *Int J Mech Mater Eng* 10 (10) (2015) 2198–2791.
- [31] O. Zobac, Experimental description of the Al-Cu binary phase diagram, *Metallurgical and Materials Transactions A* 50 (2019) 3805–3815.
- [32] J.-M. Zhang, Y. Zhang, K.-W. Xu, V. Ji, Young's modulus surface and poisson's ratio curve for cubic metals, *Journal of Physics and Chemistry of Solids* 68 (4) (2007) 503–510.  
 URL <https://www.sciencedirect.com/science/article/pii/S0022369707000133>
- [33] S. Kumar, J. Jung, Mechanical and electronic properties of Ag<sub>3</sub>Sn intermetallic compound in lead free solders using ab initio atomistic calculation, *Materials Science and Engineering: B* 178 (1) (2013) 10–21.  
 URL <https://www.sciencedirect.com/science/article/pii/S0921510712004849>
- [34] R. Hill, The elastic behaviour of a crystalline aggregate, *Proceedings of the Physical Society. Section A* 65 (5) (1952) 349–354.  
 URL <https://doi.org/10.1088/0370-1298/65/5/307>
- [35] M. de Jong, W. Chen, T. Angsten, A. Jain, R. Notestine, A. Gamst, M. Sluiter, C. K. Ande,

- S. van der Zwaag, J. J. Plata, C. Toher, S. Curtarolo, G. Ceder, K. A. Persson, M. Asta, Charting the complete elastic properties of inorganic crystalline compounds, *Scientific Data* 2 (1) (2015) 150009.  
 URL <https://doi.org/10.1038/sdata.2015.9>
- [36] N. Boudalia, J. M. Raulot, E. Patoor, C. Esling, Phase stability study of the shape memory alloy CuAl-x (x: Be, Zn, Ti, Ni, Ag and Au) by ab initio calculations, in: *THERMEC 2016*, Vol. 879 of *Materials Science Forum*, Trans Tech Publications Ltd, 2017, pp. 250–255.
- [37] T. Duguet, E. Gaudry, T. Deniozou, J. Ledieu, M. C. de Weerd, T. Belmonte, J. M. Dubois, V. Fournée, Complex metallic surface phases in the Al/Cu(111) system: An experimental and computational study, *Phys. Rev. B* 80 (2009) 205412.  
 URL <https://link.aps.org/doi/10.1103/PhysRevB.80.205412>
- [38] K. Persson, Materials data on AlCu<sub>3</sub> (SG:225) by materials project, an optional note (1 2015).  
 URL <https://materialsproject.org/docs/calculations>
- [39] X. He, L. Li, X. He, C. Xie, Multi-physical field simulation of cracking during crystal growth by bridgman method, *Materials* 16 (8).  
 URL <https://www.mdpi.com/1996-1944/16/8/3260>
- [40] J.-O. Andersson, T. Helander, L. Höglund, P. Shi, B. Sundman, Thermo-calc & dictra, computational tools for materials science, *Calphad-computer Coupling of Phase Diagrams and Thermochemistry* 26 (2002) 273–312.
- [41] K. Momma, F. Izumi, Vesta: a three-dimensional visualization system for electronic and structural analysis, *J. Appl. Crystallogr.* 41 (2008) 653–658.
- [42] S. Montecinos, A. Cuniberti, A. Sepúlveda, Grain size and pseudoelastic behaviour of a Cu-Al-Be alloy, *Materials Characterization* 59 (2) (2008) 117–123.  
 URL <https://www.sciencedirect.com/science/article/pii/S1044580306003305>
- [43] N. O. Ongwen, D. Chanbi, E. Ogam, H. O. Otunga, A. O. Oduor, Z. Fellah, Microstructural and elastic properties of stable aluminium-rich tial and tial<sub>2</sub> formed phase intermetallics, *Materials Letters* 287 (2021) 129295.  
 URL <https://www.sciencedirect.com/science/article/pii/S0167577X20320036>
- [44] N. O. Ongwen, E. Ogam, Z. Fellah, H. O. Otunga, A. O. Oduor, M. Mageto, Accurate Ab-initio calculation of elastic constants of anisotropic binary alloys: A case of FeAl, *Solid State Communications* (2022) 114879.  
 URL <https://www.sciencedirect.com/science/article/pii/S003810982200206X>